Research Square

Preprints are preliminary reports that have not undergone peer review.
They should not be considered conclusive, used to inform clinical practice,
or referenced by the media as validated information.

Wafer-Scale Synthesis of Metal-Oxide Nanonetworks for Ultra-Sensitive, Sub-Second Hydrogen Sensing Chips

Sixing Xu

xusx2021@hnu.edu.cn

Hunan University

Jiyong Zhou

Hunan University

Hui Li

Hunan University

Shunyang Zhou

Hunan University

Tianliang Meng

Hunan University

Siya Liu

Hunan University

Xiaoting Tan

Hunan University

Yuxuan Liang

Hunan University

Mingquan Zhang

Human University

Zhibiao Zhu

Hunan University

Jianyou Dai

Hunan University

Long Cheng

Hunan University

Yiliu Wang

Hunan University

Xiaohong Wang

Tsinghua University

Wenbo Ding

Tsinghua University https://orcid.org/0000-0002-0597-4512
Changsheng Wu
National University of Singapore https://orcid.org/0000-0002-0921-6356
Wanli Duan
Hunan Academy of Agricultural Sciences
Rui Li
Hunan Academy of Agricultural Sciences
Shenghua Ding
Hunan Academy of Agricultural Sciences
Qian Li
Hunan Normal University
Lei Liao
Hunan University https://orcid.org/0000-0003-1325-2410
Lei Shan
Hunan University

Article

Keywords:

Posted Date: May 13th, 2026

DOI: https://doi.org/10.21203/rs.3.rs-9342314/v1

License: This work is licensed under a Creative Commons Attribution 4.0 International License.
Read Full License

Additional Declarations: There is **NO** Competing Interest.

Wafer-Scale Synthesis of Metal-Oxide Nanonetworks for Ultra-Sensitive, Sub-Second Hydrogen Sensing Chips

Jiyong Zhou[1#], Sixing Xu[1,2#*], Hui Li[1], Shunyang Zhou[3], Tianliang Meng[3], Siya Liu[3], Xiaoting Tan[3], Yuxuan Liang[1], Mingquan Zhang[3], Zhibiao Zhu[3], Jianyou Dai[3], Long Cheng[3], Yiliu Wang[3], Xiaohong Wang[4], Wenbo Ding[5], Changsheng Wu[6], Wanli Duan[7], Rui Li[7], Shenghua Ding[7], Qian Li[8*], Lei Liao[1], Lei Shan[3*]

[1]College of Semiconductors (College of Integrated Circuits), Hunan University, Changsha, China, 410082

[2]Yuelushan Center for Industrial Innovation, Changsha, China, 410082

[3]School of Physics & Electronics, Hunan University, Changsha, China, 410082

[4]School of Integrated Circuits, Tsinghua University, Beijing, China, 100084

[5]Shenzhen International Graduate School, Tsinghua University, Shenzhen, China, 518055

[6]Department of Material Science & Engineering, National University of Singapore, Singapore 117575

[7]Dongting Laboratory, Hunan Institute of Agricultural Product Processing and Quality Safety, Hunan Academy of Agricultural Sciences, Changsha, China, 410125

[8]School of Physics & Electronics, Hunan Normal University, Changsha, China, 410081

[#]These authors contribute equally.

Correspondence and requests for materials should be addressed to S. X., Q. L. & L. S. (email: xusx2021@hnu.edu.cn, liqianl@hunnu.edu.cn, leishan@hnu.edu.cn).

Abstract

The transition to a sustainable hydrogen economy demands scalable chip-scale sensors for rapid, sensitive gas monitoring. However, current miniaturized sensors, constrained by the scarcity of high-sensitivity materials compatible with wafer-based fabrication, fall short of the critical 1 s/1000 ppm detection benchmark. Here, we overcome this barrier with a material-AI co-optimization strategy. We report a sequential hydration–dehydration process enabling the mild, in-situ synthesis of three-dimensional porous tungsten trioxide (WO_3) nanonetworks directly on wafers. This method allows for batch fabrication of sensor chips that exhibit an ultrahigh maximum response of 1.7×10^5 to 1000 ppm H_2 with sub-second response times, while achieving a scalable production cost as low as \$0.10 per chip. The formation mechanism is elucidated via in-situ characterization and density functional theory (DFT) calculations, and its generality is demonstrated by successful extension to multiple metal oxide species. Integrated with a lightweight Patch-Transformer, the chip achieves accurate concentration prediction from any 0.6 s signal segment. Leveraging its miniaturization, low power demand, and substantial room-temperature response, we demonstrate a coin-sized self-powered wireless system for real-time, non-invasive tracking of microbial hydrogen production in sealed fermenters, offering a viable path for distributed intelligent hydrogen monitoring.

Introduction

Hydrogen energy emerges as the ultimate energy solution for the 21st century, owing to its intrinsic cleanliness, sustainability, and high energy conversion efficiency[1, 2]. However, its large-scale deployment is severely hampered by the intrinsic safety hazards of hydrogen gas—namely, extreme flammability and explosiveness[3, 4]. The U.S. Department of Energy (DOE) specifies stringent hydrogen leakage detection criteria: a fast response time of <1 s and a low detection limit of 1000 ppm[5]. Consequently, it is imperative to deploy highly sensitive, rapid-response hydrogen sensing nodes on a large scale for real-time leakage monitoring. Meanwhile, given the diverse narrow, enclosed application scenarios (e.g., battery interiors, hydrogen transmission pipelines, and storage tanks), such nodes must also be highly miniaturized, wireless, and self-powered[6, 7].

Hydrogen sensor chips fabricated via advanced microfabrication processes are pivotal in this context, as they offer miniaturization, low power consumption, integrated circuit (IC) compatibility, and cost-effective manufacturability through mature semiconductor processes[8, 9]. However, within the current technological landscape, a fundamental trade-off often persists among fast response, high sensitivity, and chip miniaturization: as the sensor footprint shrinks, the available area for gas interaction diminishes, reducing the signal magnitude and signal-to-noise ratio, which in turn prolongs the time required to accumulate a detectable signal[10, 11].

To address this problem, a feasible solution is to develop ultra-sensitive materials capable of generating detectable signals within a limited chip footprint, and nanostructured metal oxides (MOS) have emerged as the leading candidate[12-14]. In particular, complex nanostructures featuring hierarchical porous architectures and 3D interconnected networks can significantly enhance the effective surface area and facilitate gas mass transport, thereby simultaneously enabling ultrahigh sensing responses and fast kinetic behavior[15, 16].

However, the on-chip integration of such materials remains challenging. Current "materials-first" synthetic approaches—including powder calcination, hydrothermal growth, and sol–gel processing[17-19]—typically entail high temperatures and the use of binders or organic additives, rendering them incompatible with the temperature and cleanliness constraints of IC fabrication processes[8]. Although MOS nanostructures can be pre-synthesized and transferred onto prefabricated wafers, they suffer from poor film adhesion and inferior wafer-scale uniformity[20]. Recent attempts to directly synthesize nanostructured materials on wafers are limited to specific material systems with low surface aspect ratio structures[21, 22], making them difficult for fabricating complex 3D open networks.

Alongside materials-driven efforts to enhance sensor sensitivity, recent work has explored computational strategies to reduce the latency of concentration estimation, an essential requirement for meeting DOE fast-response targets[23]. Machine learning approaches are particularly appealing because they can capture discriminative information from noisy, nonlinear hydrogen-sensing signals, enabling concentration prediction from short time windows[24]. Nevertheless, most existing work relies on response data collected only after exposure onset (typically restricted to the initial few seconds), which undermines their utility for genuine early warning and real-time monitoring[25, 26]. Moreover, many studies train and evaluate models using response signals drawn from the same concentration levels[27, 28]. Although the test data are never used during training, and therefore this does not constitute a conventional data-leakage issue, such protocols can still overstate performance rather than

faithfully reflect true generalization. Consequently, demonstrating robust generalization to previously unseen concentrations remain a central challenge, particularly in the low-data regime.

In this work, we address this sensor chip detection bottleneck through an intertwined material and algorithmic co-optimization strategy. First, we report a novel sequential hydration–dehydration process enabling the mild, in-situ growth of 3D porous tungsten trioxide (WO_3) nanonetworks directly on wafers, which is compatible with the CMOS process window. The formation mechanism is elucidated via in-situ characterization and DFT calculations, and the strategy is successfully extended to various other porous metal oxides (e.g., ZnO, SnO_2, CuO, In_2O_3, TiO_2), confirming its generality. The batch-fabricated WO_3-based sensor chips exhibit an exceptional response of 1.7×10^5 to 1000 ppm H_2 at 175 °C (optimum working temperature), with a substantial room-temperature response of ~ 5.1, excellent long-term stability (>60 days) and high device uniformity (relative standard deviation ≈ 4.82%), and a scalable production cost as low as $0.10 per chip. Second, based on the high-sensitivity response of the fabricated sensor chips, we implement a lightweight Patch-Transformer, which achieves accurate concentration prediction from any 0.6 s signal segment. Finally, we integrate the sensor chip with an optimized communication and energy-harvesting dual-functional wireless circuitry into a coin-sized, self-powered node, and demonstrate its utility in real-time, non-invasive monitoring of microbial hydrogen production within a sealed anaerobic fermenter. This work provides a holistic and engineer-ready solution—from material synthesis and algorithm design to system integration—paving the way for next-generation intelligent hydrogen monitoring networks.

Results

Wafer-scale synthesis of metal oxide nanostructures

Conventional nanostructured metal oxides syntheses often rely on extreme temperature and/or pressure, and may involve binders or organic additives, which complicates direct integration with CMOS process windows in terms of thermal budget and process compatibility. To overcome this fabrication bottleneck, we establish an in-situ growth route tailored for large-area integration. As shown in Fig. 1a, we propose and validate a wafer-scale in situ growth strategy for metal-oxide nanomaterials, whose core process can be described as a surface reconstruction synergistically driven by magnetron sputtering and chemical etching. Taking tungsten trioxide (WO_3) as an example, a dense WO_3 precursor film is first deposited on a silica substrate by magnetron sputtering, and the sample is subsequently exposed to a controlled acidic wet-chemical environment, where the film surface is reconstructed and hydrated intermediates (such as $WO_3\cdot H_2O$ and $WO_3\cdot 2H_2O$) are formed. During the etching step, solvent infiltration and chemical reactions act cooperatively to spontaneously transform the compact WO_3 film into a porous nanosheet architecture, thereby markedly increasing the specific surface area and exposing more reactive sites. Finally, through a mild thermal annealing step compatible with the CMOS/MEMS thermal budget ($\leqslant$ 400 °C)[29], these nanosheet structures are further crystallized to form a regularly arranged WO_3 nanosheet array. The SEM insets in Fig. 1a clearly depict the typical surface morphology evolution of the WO_3 film over the sputtering–etching–annealing sequence.

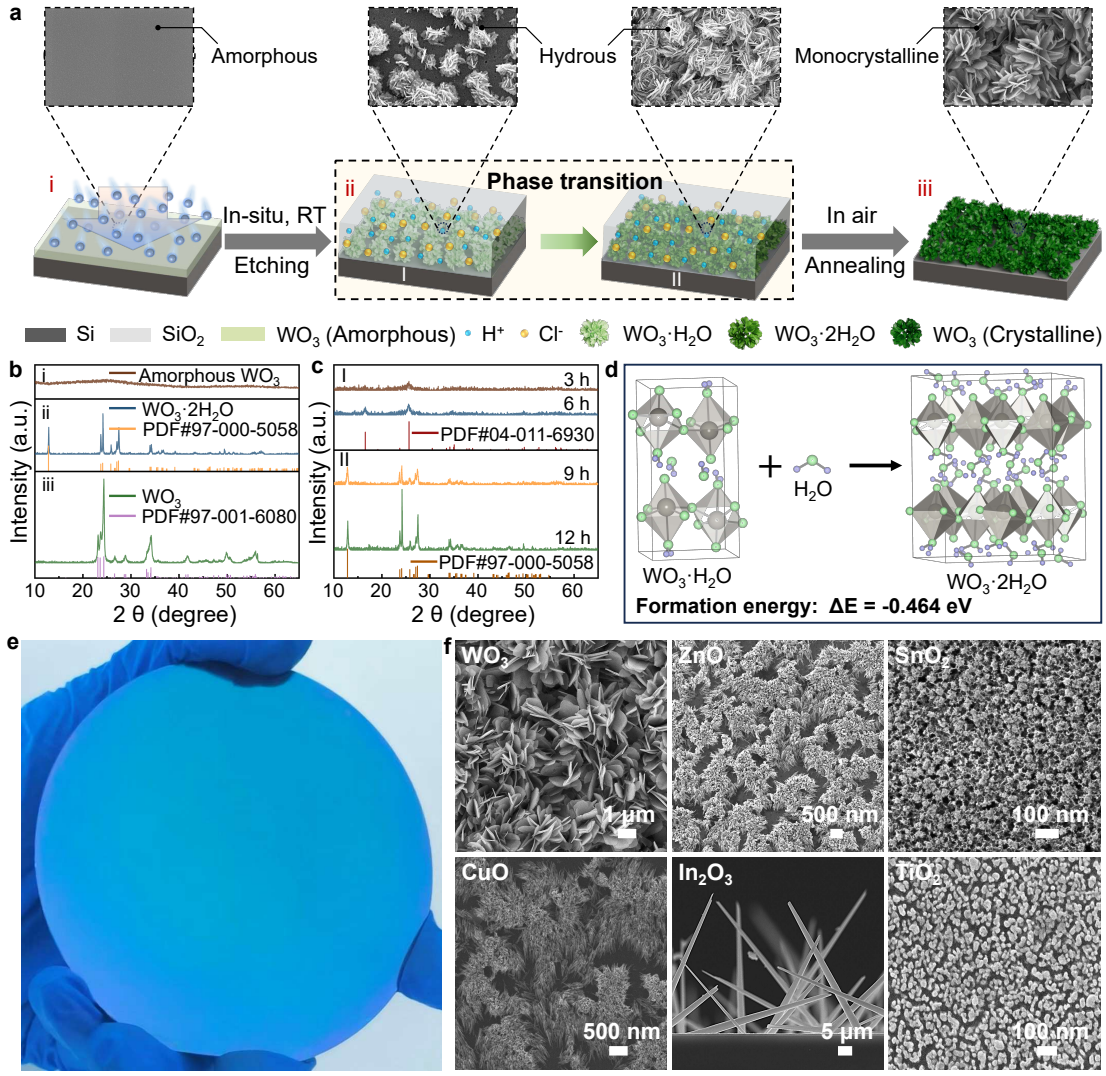


Fig. 1 | On-chip fabrication of metal oxide nanostructures. a Schematic diagram of the preparation process of WO_3 nanosheets, with inset SEM images showing the sample surface morphology at each step. **b** XRD patterns of WO_3 sensing film at various stages during preparation. **c** XRD patterns of WO_3 films at different etching times (i.e., hydration phase transition process). **d** Schematic diagram of the atomic structure of tungstite ($WO_3 \cdot H_2O$) transformed into hydrated tungsten trioxide ($WO_3 \cdot 2H_2O$) and the first-principles calculation results of the corresponding formation energy. **e** Optical images of a 4-inch wafer of nanoporous Zinc oxide. **f** SEM image of a series of metal oxide surfaces or cross-sections, such as tungsten oxide, zinc oxide, tin oxide, copper oxide, indium oxide and titanium oxide.

To elucidate the formation mechanism, we combined in situ monitoring of the surface-reconstruction process with step-resolved structural characterization at representative fabrication stages. Fig. 1b presents the X-ray diffraction (XRD) patterns of the WO_3 films at different fabrication stages. For the as-sputtered film (Fig. 1b(i)), no discernible diffraction peaks are observed, indicating an amorphous structure. After chemical etching (Fig. 1b(ii)), a series of sharp and well-defined reflections emerges, all of which can be indexed to hydrated tungsten trioxide $WO_3 \cdot 2H_2O$ (PDF#97-000-5058)[30], with no impurity peaks or secondary phases detected, confirming the formation of highly crystalline $WO_3 \cdot 2H_2O$ nanosheet precursors at this stage. Upon annealing (Fig. 1b(iii)), the film displays the characteristic

diffraction pattern of monoclinic WO_3: the main reflections at $2\theta \approx 23.11°$, 23.58° and 24.35° correspond to the (002), (020) and (200) planes, respectively (PDF#97-001-6080)[31], demonstrating that $WO_3 \cdot 2H_2O$ has been fully transformed into monoclinic WO_3 while preserving high crystallinity.

To further elucidate the structural evolution of the WO_3 films during etching, we systematically tracked samples etched for different durations by combining SEM and XRD characterization. The time-resolved SEM images in Supplementary Fig. 1 reveal that, with increasing etching time, the initially dense and flat film surface gradually evolves into a rough, porous morphology and eventually develops into a flower-like architecture assembled from nanosheets. The corresponding XRD patterns are shown in Fig. 1c, from which the entire etching process can be divided into two stages: an initial transformation from amorphous WO_3 to tungstite-type $WO_3 \cdot H_2O$, followed by a subsequent conversion from $WO_3 \cdot H_2O$ to $WO_3 \cdot 2H_2O$. As the HCl etching time is increased from 0 to 3 h and 6 h, new diffraction peaks emerge sequentially at $2\theta \approx 25.62°$ and 16.54° in the XRD patterns (Fig. 1c(I)), which can be indexed to the (111) and (020) planes of orthorhombic tungstite $WO_3 \cdot H_2O$ (space group Pmnb, PDF#04-011-6930)[32, 33], indicating the formation of a $WO_3 \cdot H_2O$ phase with still limited crystallinity. This process can be rationalized by the higher surface energy of amorphous WO_3, which facilitates its reaction with H^+ and H_2O in solution to gradually generate $[WO_2(OH)_2]$ species and, upon further hydration, octahedrally coordinated $[WO(OH)_3(H_2O)]_2(\mu\text{-}O)$ units[34]. The detailed reactions are described by Eqs. (1) and (2).

$$WO_3(\text{Amorphous}) + H_2O \xrightarrow{H^+} [WO_2(OH)_2] \quad (1)$$

$$2[WO_2(OH)_2] + 3H_2O \rightarrow [WO(OH)_3(H_2O)]_2(\mu\text{-}O) \quad (2)$$

As the etching time is further prolonged, new intense diffraction peaks emerge at 2θ = 12.88°, 23.72°, 24.18°, 25.92°, 27.48° and 37.48° in the XRD patterns (Fig. 1c(II)), which can be indexed to the (010), (001), (200), (020), (210) and (121) planes of $WO_3 \cdot 2H_2O$ (PDF#97-000-5058), respectively[30]. Concomitantly, the previously observed $WO_3 \cdot H_2O$-related reflections gradually vanish, indicating that the intermediate $[WO_3 \cdot H_2O]_n$ phase has been essentially converted into $WO_3 \cdot 2H_2O$; this phase transition can be summarized by Eq. (3).

$$[WO(OH)_3(H_2O)]_2(\mu - O) \rightarrow 2WO_3 \cdot 2H_2O + H_2O \quad (3)$$

Fig. 1d presents atomic structure models of $WO_3 \cdot H_2O$ and $WO_3 \cdot 2H_2O$ together with their formation energies calculated from first principles. The results show that the formation energy of the layered $WO_3 \cdot 2H_2O$ phase is lower than that of $WO_3 \cdot H_2O$ (see Supplementary Tab. 1), which thermodynamically explains why it is the final stable phase. The emergence of the $WO_3 \cdot 2H_2O$ phase is further corroborated by Raman spectroscopy (Supplementary Fig. 2). In addition, a comparison of the nanosheet morphologies before and after annealing (Supplementary Fig. 3) shows that the thermal treatment mainly drives the structural transition from the hydrated phase to monoclinic WO_3, while exerting only a minor influence on the overall sheet-like morphology.

To validate the generality and materials compatibility of the surface reconstruction strategy, we extended the process to a series of metal oxide thin films under comparable conditions. As shown in Fig. 1e, the optical photograph of a 4-inch ZnO wafer confirms that the nanostructured oxide layer achieves continuous coverage and visually uniform macroscopic appearance at the

wafer scale. Fig. 1f displays representative surface or cross-sectional SEM images of WO_3, ZnO, SnO_2, CuO, In_2O_3 and TiO_2 films, all of which develop distinct nanostructured morphologies, including dense granular, sheet-like and dendritic textures. To ensure that these morphological differences indeed arise from the etching-induced reconstruction rather than intrinsic deposition variations, we systematically compared the pre- and post-etching morphologies (Supplementary Fig. 4 and 5) and verified the crystal phases and bonding configurations of each system by XRD (Supplementary Fig. 6) and Raman spectroscopy (Supplementary Fig. 7). It is worth emphasizing that all oxide films are formed in situ on the wafer without any transfer or bonding steps, thereby ensuring robust film–substrate adhesion and compatibility with subsequent microfabrication processes. Collectively, these results demonstrate that the proposed in situ strategy possesses excellent scalability and versatility across both materials space and wafer-level dimensions.

Fabrication and characterization of WO_3-based sensor chip

To maximally expose the WO_3 nanosheets to the ambient atmosphere, we finely tuned the overall post-etching morphology by varying the sputtering duration (that is, the deposited amount of WO_3; nanoscale morphologies at different sputtering times are shown in Supplementary Fig. 8), thereby constructing a nanostructured sensing layer with well-defined gas pathways. As illustrated in Fig. 2a, the microchannel design allows gas molecules to fully access the sensing surface, reducing "dead" regions in the material and thus increasing the probability of gas adsorption and surface reactions. By creating explicit gas flow paths within the sensitive layer, the microchannel architecture effectively lowers diffusion resistance, enabling gas molecules to reach and leave the sensing interface rapidly and efficiently, which in turn shortens the response/recovery times and enhances the detection performance[4]. Building on this, to accelerate the surface-reaction kinetics of WO_3-based films toward hydrogen, we decorate the WO_3 nanosheet nanonetwork with PdO nanoparticles to form PdO/WO_3 heterointerfaces and to promote hydrogen-related surface processes (for example, adsorption/dissociation and interfacial charge modulation), thereby further amplifying the chemiresistive response. The complete microfabrication process of the PdO/WO_3 sensor is described in the Methods section and in Supplementary Fig. 9. As shown in Fig. 2b, 1088 sensor devices are integrated on a 4-inch wafer, demonstrating excellent wafer-level integration and strong potential for industrial-scale batch production. Fig. 2c compares the footprint of a single sensor (area $\approx 2.3 \times 2.4$ mm^2) with a grain of rice, highlighting its pronounced miniaturization and suitability for microsystem integration. Supplementary Fig. 10 presents the element distribution of an individual device obtained from energy-dispersive X-ray spectroscopy (EDS).

Figure 2d shows the surface morphology of the sensing chip, while Supplementary Fig. 11 presents the corresponding cross-sectional view. Together, these images indicate that the in situ grown WO_3 nanosheets adopt a well-defined plate-like morphology with a relatively uniform lateral size distribution, forming large-area, homogeneous nanosheet arrays on the Si substrate. The surface elemental composition of PdO/WO_3 nanosheets at different Pd sputtering times was analyzed by EDS (Supplementary Fig. 12 and 13). As the Pd sputtering time increases from 5 s to 25 s, the Pd atomic fraction in the WO_3 film increases approximately linearly from ~0.6 at% to ~3.1 at% (Supplementary Table 2 and Supplementary Fig. 14), confirming that this process enables stable and precisely tunable Pd loading. The cross-sectional TEM image of the PdO/WO_3-20s heterostructure film (where "20s" denotes a Pd sputtering

time of 20 s) in Supplementary Fig. 15 further reveals a layered architecture composed of the WO_3 nanosheet backbone decorated with surface nanoparticles. Representative EDS elemental maps (Figure 2e–h) show strong W and O signals and a weaker yet uniformly distributed Pd signal, demonstrating that Pd-based nanoparticles are highly dispersed on the WO_3 nanosheet surface, thereby forming a continuous and finely dispersed PdO/WO_3 heterointerface. Such nanoscale noble-metal/metal-oxide junctions have been identified as key structural motifs for enhancing hydrogen sensing performance[35]. High-resolution TEM (HRTEM) images (Figure 2i) provide further insight into the local crystal structure. The WO_3 nanosheet region exhibits clear lattice fringes with an interplanar spacing of ~0.367 nm, consistent with the (200) plane of monoclinic WO_3[36], while the lattice spacing of the supported nanoparticles is ~0.263 nm, corresponding to the (101) plane of PdO[37].

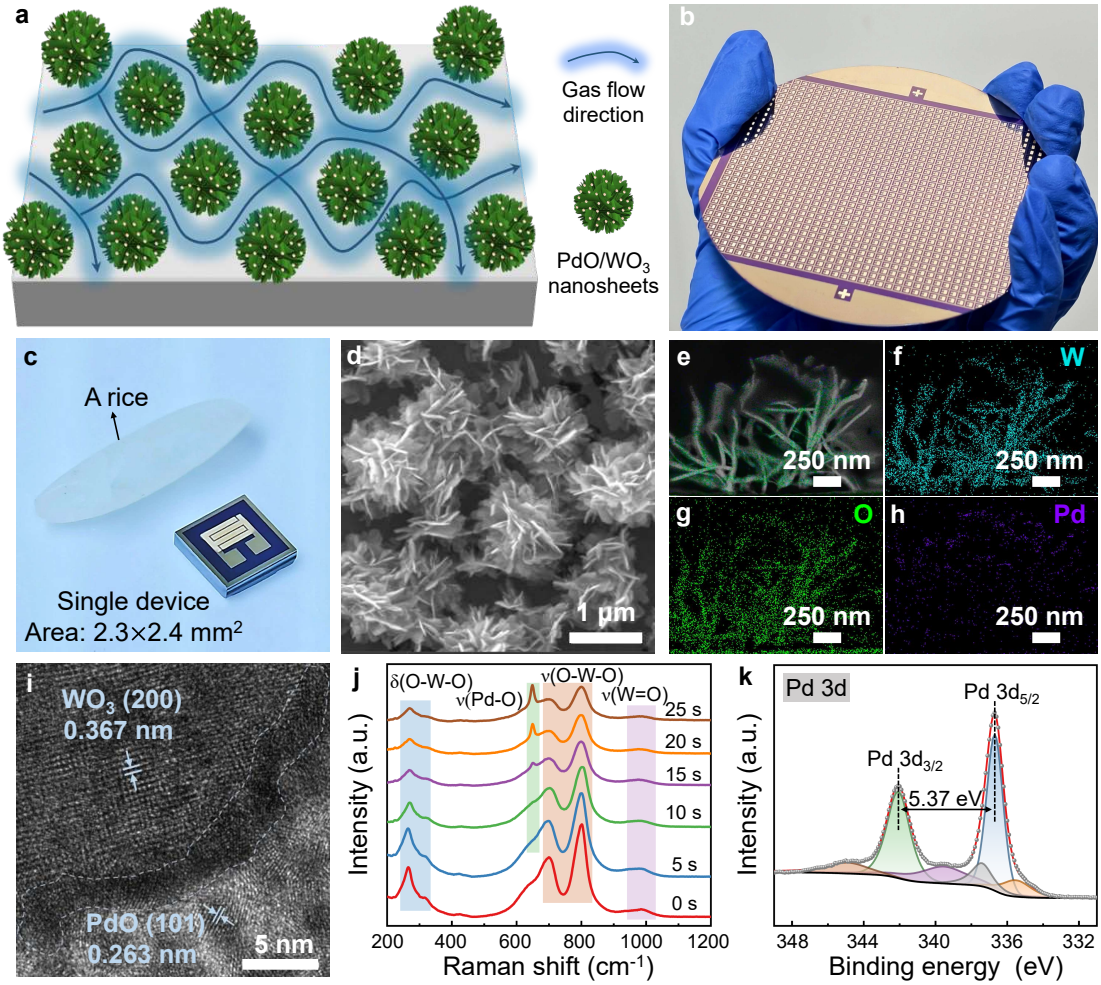


Fig. 2 | Morphology and phase characterizations of PdO/WO_3-20s sensor chip. a Schematic illustration of the engineered microchannels, which enable sufficient contact between the H_2 gas and the sensing material. **b** Optical picture of the 4 inches wafer (1088 sensor chips). **c** Single sensor chip compared with a grain of rice. **d** Surface morphology of the PdO/WO_3-20s sensor chip. **e-h** Elemental mapping images of W, O, and Pd elements in PdO/WO_3-20s nanosheets. **i** HRTEM images of PdO/WO_3 nanosheets. **j** Raman spectra of WO_3 and PdO/WO_3 (different Pd deposition times) at 200 – 1200 cm^{-1}. **k** XPS spectra of Pd 3d of the PdO/WO_3-20s nanosheets.

The XRD patterns of pristine WO_3 and PdO/WO_3-20s films were both shown in Supplementary Fig. 16. In the Raman spectra (Fig. 2j), the bands at 269 and 322 cm^{-1} are assigned to O–W–O bending modes, those at 704 and 805 cm^{-1} to O–W–O stretching modes, and the weak feature near 975 cm^{-1} to the stretching vibration of terminal W=O bonds, consistent with the characteristic vibrational fingerprints of monoclinic WO_3[38, 39]. With increasing Pd loading, the WO_3-related bands exhibit a slight blue shift, and a broad band emerges and gradually intensifies around ~650 cm^{-1}, which can be attributed to Pd–O stretching modes of PdO[40]. At the same time, the overall Raman intensity of the WO_3 modes decreases as the Pd loading increases. This behaviour is likely associated with the formation of O–W–O–Pd^{2+} bridge structures upon PdO modification of the WO_3 surface, which perturb the local coordination environment of the W–O–W network and introduce lattice strain, thereby increasing local lattice rigidity and suppressing the vibrational amplitude[16, 41]. High-resolution XPS analysis (Fig. 2k and Supplementary Fig. 17 & Supplementary Table 3) further corroborates these findings. In PdO/WO_3-20s, the W 4f doublet shifts to higher binding energy compared to pristine WO_3, and the relative fractions of oxygen-vacancy and chemisorbed-oxygen components in the O 1s spectrum increase markedly, while the Pd 3d spectrum reveals the coexistence of Pd^0, Pd^{2+} and Pd^{4+} species[42-44]. These results indicate that introducing Pd markedly increases the abundance of defect-related oxygen and chemisorbed oxygen species at the surface. Such surface-active oxygen species are widely recognized as the key sites for charge exchange with target gases such as H_2 in metal-oxide-based gas-sensing reactions, and can substantially amplify the resistance change by modulating the thickness of the surface depletion layer[45, 46]. Quantitative peak deconvolution (Supplementary Table 4) shows that Pd exists mainly in the Pd^{2+} (PdO) state, accompanied by minor Pd^0 and Pd^{4+} contributions, giving rise to a Pd^0–PdO–WO_3 multiphase heterogeneous interface. This multiphase interface not only provides efficient pathways for H_2 adsorption–dissociation and O^{2-}/O^- spillover, but also modulates carrier transport via p–n heterojunction formation and band bending, thereby cooperatively enhancing the impact of surface active oxygen on conductivity modulation and rationalizing the markedly improved H_2 response of PdO/WO_3-20s compared with the pristine WO_3 film[47, 48].

Gas sensing performance

To evaluate the advantages of the materials prepared by this method for H_2 detection, we fabricated a series of PdO/WO_3-based sensor chips and performed systematic measurements. We first determined the optimum working temperature (OWT) by measuring the response of each device to 1000 ppm H_2 over 150–250 °C. As shown in Fig. 3a, all devices exhibit a volcano-type temperature dependence, with the response increasing and then decreasing as the temperature rises. Among them, PdO/WO_3-20s reaches its maximum response at 175 °C, with $Ra/Rg \approx 1.7 \times 10^5$. Considering the demand for rapid readout in hydrogen safety monitoring, we further examined the temperature dependence of the sensing kinetics (Supplementary Fig. 18). At 1000 ppm H_2, the response time decreases from 4.4 s at 150 °C to ~2.3 s at ≥175 °C and remains essentially unchanged at higher temperatures, indicating that fast kinetics is already achieved at 175 °C, whereas further heating provides no additional acceleration and reduces the response magnitude. Therefore, we selected 175 °C as the OWT for PdO/WO_3-20s. In addition, to assess operation without external heating, we conducted room-temperature measurements under air and nitrogen backgrounds (Supplementary Fig. 19). At room

temperature, the sensor still delivers a response of 5 (air) and 8.4 (N_2) to 1000 ppm H_2, demonstrating appreciable room-temperature sensing capability under different background gases and providing experimental support for subsequent low-power applications. We then evaluated the concentration-dependent response at 175 °C. Figure 3b and Supplementary Fig. 20 show the dynamic response–recovery curves in the ranges of 50–1000 ppm and 1–10 ppm H_2, respectively, where the response increases monotonically with increasing H_2 concentration. The lowest tested concentration reaches 1 ppm, corresponding to a response of ~1.24. Figure 3c and Supplementary Fig. 21 plot the log–log relationship between response and concentration; the results reveal an approximately linear dependence in both the high- and low-concentration regimes (the fitting equation and R^2 are provided in the inset), indicating that the device enables quantitative readout over a wide concentration range.

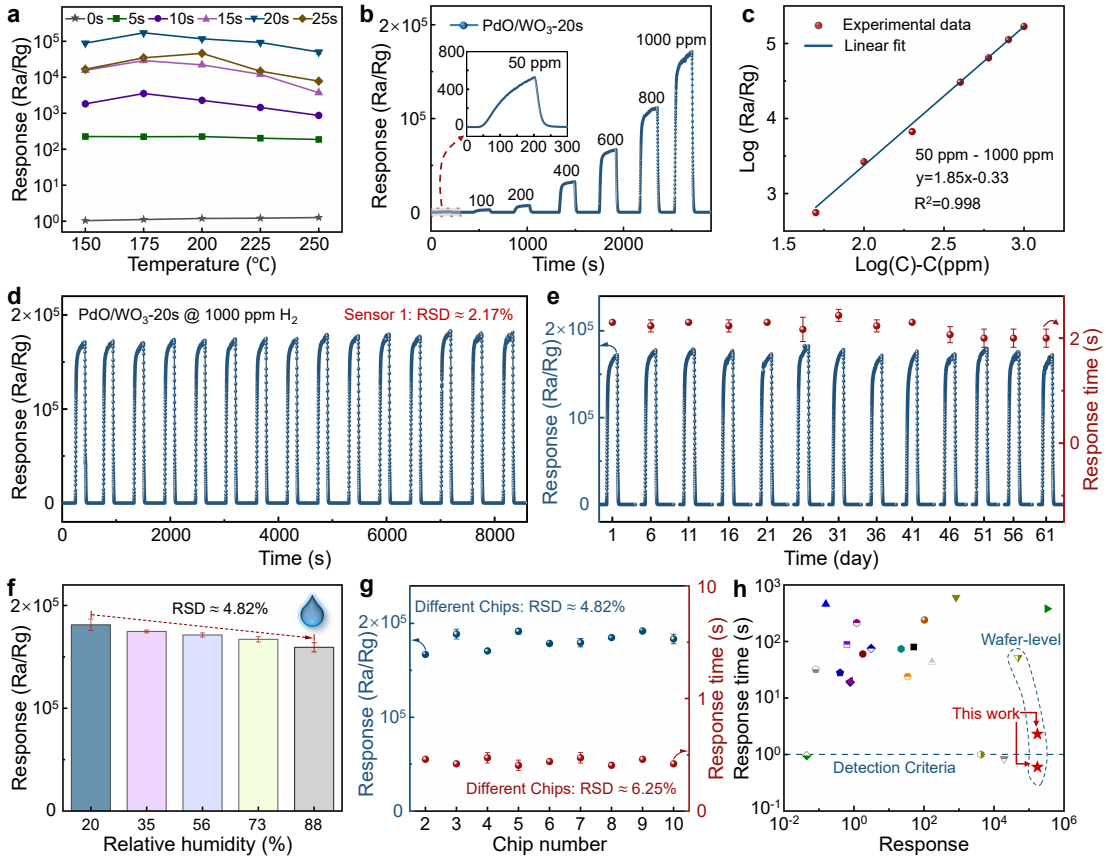


Fig. 3 | Performance characteristics of different PdO/WO_3-based sensor chips under various conditions. a Temperature-dependent responses of the different PdO/WO_3-based sensor chips to 1000 ppm H_2. **b** The dynamic response-recovery curves of PdO/WO_3-20s sensor chip to different concentrations (50-1000 ppm) of H_2 at 175 °C, **c** corresponding log (Ra/Rg)-log(C) fitted curves (The unit of C is ppm). **d** The 15-cycle dynamic sensing response of PdO/WO_3-20s sensor chip to 1000 ppm H_2 at 175 °C. **e** The response and response time of the PdO/WO_3-20s sensor chip to 1000 ppm H_2 at 175 °C for 2 months. **f** The effect of different relative humidities (RH) on the response of the PdO/WO_3-20s sensor chip. **g** Response and response time measured across different chips (RSD ≈ 4.82% and 6.25%). **h** Performance comparison with prior studies under 1000 ppm H_2, with this work indicated.

In addition, the cycling stability of the sensors at 175 °C was evaluated by repeatedly exposing them to 1000 ppm and 10 ppm H_2 for 15 successive cycles at each concentration. As

shown in Fig. 3d, the peak response remains essentially unchanged throughout the cycling tests, with a relative standard deviation (RSD) of ≈ 2.17%, indicating excellent cycle-to-cycle stability of our devices. To further assess long-term stability, the PdO/WO_3-20s sensor was continuously tested toward 1000 ppm H_2 at 175 °C over a period of 61 days (Fig. 3e and Supplementary Fig. 22). The average response and response time over the entire test window are 1.7×10^5 and 2.3 s, respectively, with corresponding RSD values of ≈ 2.59% and ≈ 6.39%, demonstrating outstanding long-term stability for H_2 detection. Since ambient humidity can influence gas-sensing performance, we further evaluated the sensor response under different relative humidity (RH) levels. As shown in Fig. 3f and Supplementary Fig. 23, the response to 1000 ppm H_2 was recorded at 20%, 35%, 56%, 74%, and 88% RH, and the RSD of the response across these humidity conditions is ≈ 4.82%, indicating that the sensor performance is only weakly affected by humidity.

In practical applications, high selectivity is also a key performance target for gas sensors. To this end, we evaluated the selectivity of the PdO/WO_3-20s sensor at 175 °C against typical interfering gases, including methanol, ethanol, acetone, N, N-dimethylformamide, isopropanol and ethylene glycol (all at 1000 ppm). As shown in Supplementary Fig. 24, the PdO/WO_3-20s sensor exhibits an ultrahigh response to H_2 compared with the other gases at the same high concentration, demonstrating good selectivity toward H_2. This behaviour may arise from the lower bond dissociation energy and smaller kinetic diameter of H_2, which make it more prone to diffusion and surface reaction than the other analytes. We further verified device-to-device reproducibility. First, nine gas sensors were selected from different regions of the same wafer for surface morphology characterization. All sampled regions show the same loosely packed nanosphere-like architecture composed of WO_3 nanosheets (Supplementary Fig. 25), further supporting the wafer-scale uniform synthesis of the PdO/WO_3 nanonetworks. Next, these nine sensors (n=9) were individually evaluated in gas-sensing measurements (Fig. 3g). The sensors exhibit low RSDs (≈ 4.82% and 6.25%, respectively) in both the response and response time to 1000 ppm H_2, indicating high performance uniformity across the wafer. Finally, cycling stability tests were performed for this set of PdO/WO_3-20s sensors, all of which show excellent cycling stability (Supplementary Fig. 26). Compared with previously reported wafer-scale gas sensors (Supplementary Fig. 27 and Supplementary Table 5), our devices exhibit highly uniform response characteristics across different units on the same wafer, evidencing excellent device-to-device reproducibility. A further comparison with representative hydrogen-sensing technologies (Fig. 3h and Supplementary Table 6) shows that, while maintaining a simple fabrication flow that is readily compatible with existing CMOS processes, the present sensor still offers pronounced advantages in key performance metrics, including response magnitude and response time. Collectively, these attributes underscore the strong potential of this technology for high-yield, low-cost, wafer-level mass production of MEMS gas sensors.

Taken together, these results demonstrate that the PdO/WO_3-20s sensor chip simultaneously meets practical requirements in terms of sensitivity, selectivity, cycling stability, and device-to-device consistency. Its outstanding performance can be attributed to several synergistic factors, including optimized operating temperature, nanoscale structural effects, the catalytic spillover effect of PdO, and the formation of p–n junctions between PdO nanoparticles and WO_3 nanostructures. In addition, the engineered microchannel architecture within the sensing layer plays a crucial role in enhancing gas transport and reaction efficiency. A detailed

discussion of the sensing mechanism is provided in Supplementary Fig. 28.

Machine learning boosted sub-second gas concentration prediction

Conventional concentration readout typically requires waiting for the sensor signal to settle sufficiently to support a reliable estimate, introducing latency that conflicts with DOE sub-second response targets[5]. To support sub-second detection of H_2 concentration levels and seamless real-time monitoring, we adopt a Transformer-based approach[49] that predicts concentration end-to-end from randomly sampled short segments of the ongoing response stream, simulating the incomplete observations encountered in real-time monitoring, as illustrated in Fig. 4a. By virtue of the chip sensor's high signal fidelity, the resulting model generalizes well to previously unseen concentration levels, improving practicality in real-world use cases.

Specifically, we first construct the dataset using a sliding-window strategy that partitions each continuous response trace into fixed-duration segments (Methods). Each randomly sampled segment is then divided into smaller patches before being sent to the Patch-Transformer. This patching strategy encourages the model to exploit local temporal structure while substantially reducing the token sequence length for self-attention, improving computational efficiency and predictive performance. Subsequently, a 1D convolution encoder maps each patch to a high-dimensional embedding, followed by positional encodings to preserve the original time order. Stacked Transformer layers then learn concentration-relevant dependencies across patches and iteratively refine the latent representations. The final concentration value is produced by an MLP prediction head.

Notably, concentration inference exhibits an intrinsic speed-accuracy tradeoff: longer observation windows generally improve prediction accuracy, yet increasing the window length conflicts with DOE sub-second response targets. This trend is displayed in Fig. 4b, where progressively longer segment windows yield higher accuracy. Importantly, owing to the Patch-Transformer's effectiveness in modeling time-series signals, the R^2 metric approaches saturation at a 0.6-second window, with only marginal improvements for longer windows. This behavior indicates that a 0.6 s segment already captures sufficient information to enable reliable sub-second quantification. Furthermore, to assess the model's generalization to previously unseen concentration levels, we adopted a concentration-holdout protocol, in which a subset of concentrations in the test set was withheld entirely from training and validation (Supplementary Table 7). As shown in Fig. 4b, when 30% and 40% of concentrations are unseen during training, the R^2 only decreases slightly compared to the *Regular* setting, in which all test concentrations are represented in the training set, indicating non-trivial generalization of the model.

Under the *Regular* setting, the model converges after around 100 epochs with no pronounced signs of overfitting, as manifested in Fig. 4c. The Patch-Transformer consistently achieves higher predictive performance on randomly sampled 0.6 s segments than representative CNN, LSTM, Transformer, and hybrid baselines[50-53] (Fig. 4d and Supplementary Fig. 29-35), highlighting the advantage of patch-based modeling for sub-second prediction. Overall, the joint optimization of a Patch-Transformer and the fast kinetics of the sensing chip not only enables sub-second quantification but also establishes a viable framework for early-warning operation and continuous real-time monitoring.

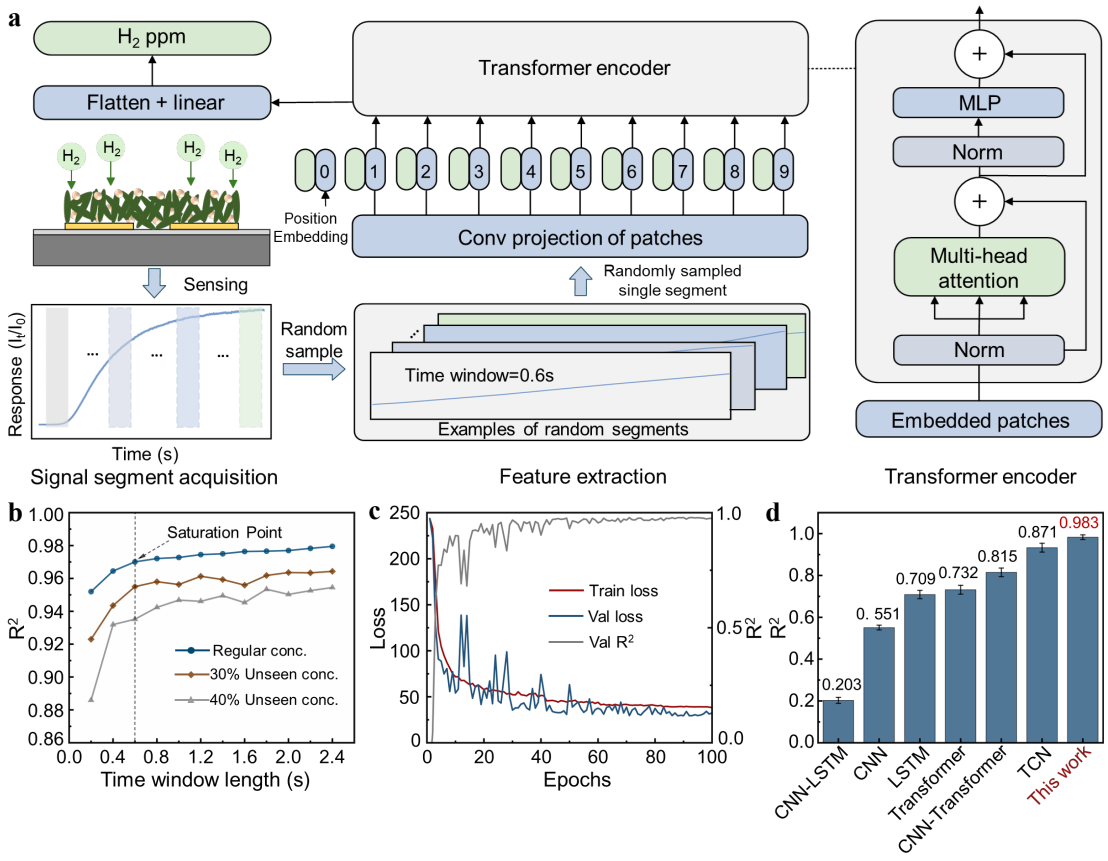


Fig. 4 | Machine learning strategy for rapid gas concentration prediction. a Schematic of the adapted Patch-Transformer architecture and its training pipeline. b Trade-off between input window length and predictive performance (R^2) under different holdout protocols. Regular conc. denotes that all concentration levels are present in the training/validation/test sets. ***30% Unseen conc.*** and ***40% unseen conc.*** denote that 30% and 40% of testing concentration levels are excluded from the training stage, respectively. The dashed line marks the 0.6 s saturation point where performance gains begin to saturate. c Training curves of training/validation losses and validation-R^2 over epochs. d Benchmark comparison. The R^2 of the proposed model versus representative baselines (CNN, LSTM, Transformer, and hybrid variants).

Wireless, self-powered sensor node for biological hydrogen production monitoring

Growing demand for sustainable energy, together with escalating environmental pressures associated with fossil fuels, has positioned biohydrogen as a promising renewable energy pathway[54]. Microbial fermentation can convert organic wastes into hydrogen, enabling simultaneous waste valorization and clean-fuel generation while potentially reducing greenhouse-gas emissions and the burden of end-of-pipe treatment[55, 56]. In biohydrogen-producing microbial consortia, many high-performing strains are obligate or facultative anaerobes, and their key hydrogen-producing enzyme systems are highly oxygen-sensitive. Even minor oxygen ingress during sampling, bottle opening, or offline analysis can perturb the anaerobic microenvironment and suppress enzymatic activity, leading to reduced biohydrogen production rates and, in severe cases, loss of microbial viability[57]. These constraints motivate non-invasive, in situ monitoring strategies that avoid oxygen introduction and preserve strictly anaerobic conditions. Here we develop a miniaturized, wireless hydrogen-monitoring system

based on a PdO/WO_3 hydrogen sensor, which markedly reduces the device footprint while enabling simultaneous wireless power delivery and data communication for fine regulation and rapid screening of hydrogen-producing microbial (Fig. 5a). Using a printed circuit board (PCB) platform, we integrate the PdO/WO_3-20s sensor chip with multifunctional circuitry at the system level, yielding a coin-sized module that can be mounted directly on the culture-bottle cap for continuous, in situ measurements (Fig. 5b). The wireless monitoring system comprises a master circuit, a slave circuit, a readout circuit and a mobile terminal, as illustrated in (Fig. 5c). The slave and readout circuit integrates a rectification module, a low-dropout regulator (LDO), the hydrogen sensor, enabling reception of magnetically coupled power and acquisition of the sensing signal, while using the readout output as a modulation signal for backscatter transmission. The master circuit delivers wireless power to the slave circuit via magnetically coupled resonance and simultaneously demodulates the modulated signal. An FPGA and a Bluetooth communication module enable wireless data transmission and real-time display between the device and a smart terminal. Detailed information on the PCB design and the customized mobile application is provided in the Methods section.

The wireless monitoring platform enables systematic evaluation of the effects of sheep blood supplementation, cultivation temperature, and bacterial concentration on the hydrogen-production efficiency of anaerobic bacteria, with the results displayed in real time by the mobile monitoring software (Fig. 5d). Baseline output tests of multiple wireless monitoring systems prior to cultivation showed that the initial system outputs were highly overlapping with minimal fluctuations across systems, demonstrating good inter-system consistency (Supplementary Fig. 36). In addition, response curves under different growth conditions were recorded using the proposed monitoring platform. (Fig. 5e). Comparative experiments under different cultivation conditions revealed that Cond.3 (37 °C, sheep blood supplementation, inoculum dilution 1:100) delivered the best performance, exhibiting the fastest onset of hydrogen production and the highest hydrogen evolution rate, with the output current reaching 236 nA and approaching the upper limit of the system output range. Detailed information on the biohydrogen production protocol and cultivation condition settings is provided in the Methods section. To validate measurement reliability, a commercial hydrogen sensing device was employed for comparative monitoring. The results show strong agreement between the wireless system and the industrial device in both response trends and concentration variations, confirming the accuracy of the proposed system in practical biohydrogen monitoring scenarios. In addition, leveraging the PdO/WO_3-20s sensor, a hydrogen leakage alarm system was implemented for environmental hydrogen safety monitoring (Supplementary Fig. 37, 38 and Supplementary Video). Overall, this wireless hydrogen monitoring system demonstrates a high level of system integration and engineering practicality in continuous in situ monitoring, wireless power delivery, data transmission, and regulation of biohydrogen production processes, providing a promising solution for the safe operation and scalable deployment of hydrogen production technologies.

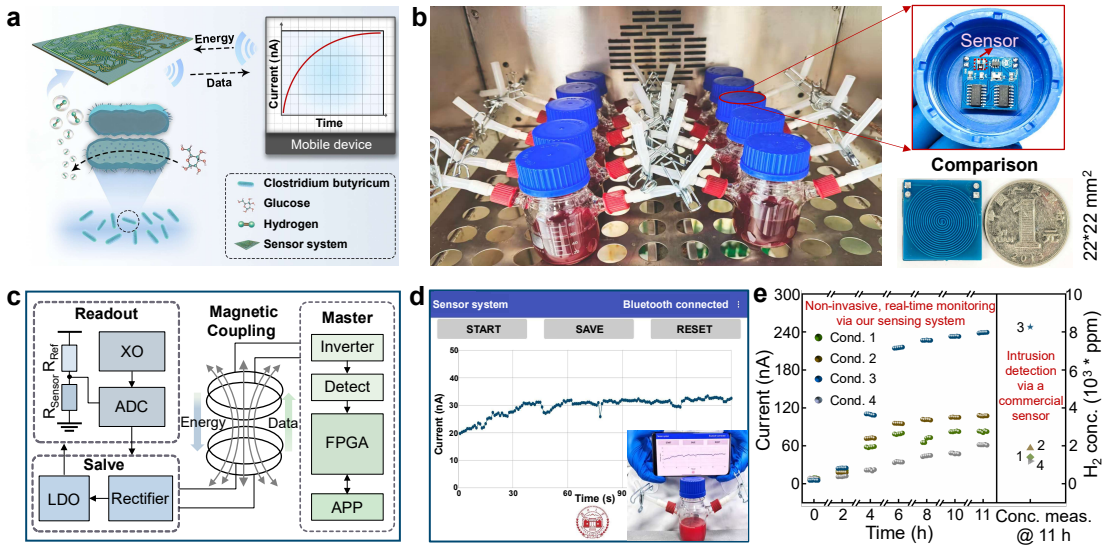


Fig. 5 | Miniaturized wireless hydrogen sensor based on PdO/WO_3 for real-time monitoring of biological hydrogen production process. a Schematic diagram of real-time monitoring of the biological hydrogen production process. b Photograph of the biohydrogen production experimental setup and the corresponding modules (the slave and readout circuits are embedded in the bottle cap and occupy only 22 × 22 mm^2). c Block diagram of the entire magnetically coupled resonant wireless energy and data transmission system. d A representative screenshot of the mobile terminal interface for data acquisition during the field test (inset, photograph of the mobile terminal). e Response curves under different growth conditions, showing excellent agreement with a commercial hydrogen sensor.

Discussion

In summary, we report a materials–algorithm co-optimization strategy to overcome the H_2 sensor chip detection bottleneck. We develop a mild, CMOS-compatible, wafer-scale sequential hydration–dehydration route—implemented via magnetron sputtering, controlled wet-chemical etching, and annealing—that enables the in-situ growth of WO_3 nanosheets directly on wafers. By integrating systematic characterization with DFT calculations, we elucidate the phase/structure evolution from an amorphous precursor through hydrated intermediates to monoclinic WO_3, and further demonstrate the transferability of this fabrication paradigm across multiple metal-oxide systems (ZnO, SnO_2, CuO, In_2O_3 and TiO_2). Batch-fabricated PdO/WO_3 sensor chips exhibit an ultrahigh response of ~1.7 × 10^5 to 1000 ppm H_2 at 175 °C, together with a substantial room-temperature response (~5.1), excellent long-term stability (>60 days), and high device-to-device uniformity (relative standard deviation ≈ 4.82%), while achieving a scalable production cost as low as $0.10 per chip. Leveraging the strong transient sensitivity of the devices, we develop a lightweight Patch-Transformer model optimized for non-equilibrium transient segments, enabling accurate concentration regression from any 0.6 s signal snippet in offline evaluation and thereby supporting sub-second early readout without waiting for steady-state responses. Meanwhile, by integrating the sensor chip with optimized dual-functional wireless circuitry for energy harvesting and data communication into a coin-sized self-powered node, we demonstrate real-time, non-invasive monitoring of microbial hydrogen production in a sealed anaerobic fermenter. Importantly, the mild processing conditions and excellent CMOS compatibility of our method lay the groundwork for seamless embedding of nanostructured

sensors into standard microelectronic flows and for their large-scale manufacturing. We anticipate that the synergy of ultra-high sensitivity, low-power operation, and AI analytics will position this platform for broad deployment in implantable health monitoring, smart agriculture, and industrial process safety, and will help drive the development of a new generation of scalable, intelligent sensing systems.

Methods

Fabrication of the PdO/WO_3 sensor chip

The fabrication process for the on-chip PdO/WO_3 sensor chip, as shown in the flowchart in Supplementary Fig. 9. First, photoresist is patterned on a SiO_2 (300 nm)/Si (500 μm) substrate to form an interdigitated structure (with a width of 150 μm and an electrode gap of 50 μm). Cr/Au (10/40 nm) is then evaporated as the current collecting layer, and then lift-off is performed to form the interdigitated electrodes. Next, the sensing layer material was patterned (1.3 mm in length and 0.75 mm in width) onto the Au/Cr/SiO_2/Si substrate by overlaying. Subsequently, a WO_3 layer was deposited onto the substrate using DC reactive magnetron sputtering from a 2-inch WO_3 target (99.99% bonded to a 2-mm-thick copper backing target) in an Ar/O_2 atmosphere. Before deposition, the chamber base pressure was maintained at approximately 9.8×10^{-6} mbar, and the target-substrate distance was fixed at 8.5 cm. Sputtering parameters were set as follows: process pressure of 5×10^{-3} mbar, Ar/O_2 gas ratio of 40/4 sccm, target power density of 3.0 W cm^{-2}, deposition temperature of room temperature, stage rotation speed of 20 rpm, and deposition time of 15 min. The resulting film was then chemically etched with a 0.5 mol L^{-1} hydrochloric acid solution for 12 hours, slowly forming a $WO_3 \cdot 2H_2O$ nanosheet structure. Pd catalyst nanoparticles were then deposited onto the nanosheets using conventional DC magnetron sputtering using a 2-inch Pd target (99.99%) at room temperature. To ensure uniform Pd deposition on the nanosheets, the sample stage was rotated at 40 rpm. The Pd deposition time was varied from 5 to 25 seconds to control the density of the Pd nanoparticles. To distinguish different Pd loadings, samples are denoted as PdO/WO_3-*t*s throughout this work, where *t* is the Pd sputtering time (in seconds); for example, PdO/WO_3-20s refers to the sample obtained with a Pd sputtering time of 20 s. The sensor device was then formed using a lift-off technique. Finally, the device was annealed at 400 °C in air for 2 hours.

Characterization

The sample planar and cross-sectional morphologies were characterized using scanning electron microscopy (SEM, TESCAN). The surface crystal composition of the sample was determined using X-ray diffraction (XRD, Smartlab SE). Cross-sectional slices were prepared using an in-situ extraction process using a focused ion beam scanning electron microscope (FIB-SEM, TESCAN AMBER). The cross-sections of the FIB films were characterized by transmission electron microscopy (TEM, JEOL JEM-F200). Raman spectroscopy (Raman, Thermo Scientific-DXR3) was used to examine the chemical bond types of the composites. The elemental composition and chemical state of the sample surface were analyzed using an X-ray photoelectron spectrometer (XPS, Thermo Scientific K-Alpha+) under ultrahigh vacuum conditions with an Al Kα radiation source, and the binding energy was based on the C 1s peak (284.8 eV).

Hydrogen sensor performance test method

In this work, we adopted a method combined with a dynamic gas mixing system (Supplementary Fig. 39). The measurements were performed in a closed chamber consisting of a sample stage and temperature controller. The flow rates of hydrogen and dry air (used as background gas) were monitored by a KT-C2ZS multi-channel mass flow controller. All measurement gases were purchased from Hunan Changfei Gas Equipment Trading Co., Ltd. and had standard gas manufacturing percentages. The sample stage's operating temperature is controlled by a temperature controller purchased from Zhengzhou Ketan Instruments Co., Ltd., which allows for real-time adjustment and control of sample temperature. Gas humidification is achieved via bubbling. Specific parameters are shown in Supplementary Table 8 and Supplementary Fig. 40. The real-time resistance value is recorded by a computer connected to a Keithley 2635B source meter, with a bias voltage of 2 V applied during the measurement. For reducing gases such as hydrogen, the sensor response is defined as in Eq. (4).

$$\text{Response} = \frac{R_a}{R_g} \tag{4}$$

Where R_a is the base resistance of the sensor in air, and R_g is the resistance measured in the presence of a reducing gas. The response time (t_{res}) and recovery time (t_{rec}) are defined as the time required for the gas sensor's resistance change to reach 90% of its final equilibrium state when the target gas is injected and exhausted, respectively.

Data acquisition and dataset construction

Gas-sensing experiments were conducted in a dynamic test system using a Keithley Instruments 2636B source meter. The sensor was operated at a constant temperature of 175 °C under a 2 V bias, and the current response was recorded at a sampling rate of 15 Hz. The dataset spans ten concentration levels from 100 to 1000 ppm; to capture diverse kinetic characteristics, the 100 ppm condition was measured five times, while each of the remaining concentrations (200–1000 ppm) was measured ten times, yielding 95 raw time-series trials. In preprocessing, each trial was first truncated to a 180 s window starting from the onset of gas exposure (time zero) and then time-zero aligned. To obtain a strictly uniform sampling grid after alignment, signals were resampled onto a fixed 15 Hz grid via linear interpolation. The response was baseline-normalized as $I_{rel}(t)=I(t)/I_0$, where I_0 denotes the pre-exposure baseline current. For stable model training, concentration labels were normalized to the [0, 1] range by dividing by the maximum concentration (1000 ppm). To emulate fragmented observations and enable early-readout learning, each 180 s response curve was segmented using a sliding-window strategy into short-time fragments of length 0.6 s (9 samples at 15 Hz). For the training set, we used an overlapping stride of 5 samples (~0.33 s) to increase segment diversity and better capture transient dynamics; for the validation and test sets, we used a non-overlapping stride of 9 samples (0.6 s) to ensure that segments within each trial do not overlap. We performed a stratified 6:2:2 split by concentration across raw response files, and applied sliding-window segmentation after the split. Consequently, training, validation, and test segments were generated from non-overlapping files, avoiding cross-set leakage. Each holdout type therefore comprised 2 (withheld sets) × 2 (random seeds) = 4 runs, and performance was reported as the mean across runs; for the standard (non-holdout) setting, we evaluated four random seeds and reported the mean performance.

Model architecture and training

We implemented a tailored Patch-Transformer to decode 0.6 s single-channel sensor segments. The input $X \in R9\times1$ is first passed through a patch embedding layer (1D convolution, kernel size = 3, stride = 3) to project it into a high-dimensional latent space. This operation "tokenizes" each segment into three non-overlapping patches with an embedding dimension of 128, followed by learnable positional encodings to preserve temporal information. The encoder consists of four Transformer blocks, each comprising 4-head multi-head self-attention and a feed-forward network with an expansion ratio of 4. We adopt a Pre-Norm configuration[58] with Gaussian Error Linear Units (GeLU) as the activation function[59]. The resulting patch features are then flattened and passed through a linear regression head to output the predicted concentration. The total number of trainable parameters is about 0.79 M. The model is implemented in PyTorch and trained on an NVIDIA RTX 4090 GPU using the AdamW optimizer[60] (initial learning rate 1×10^{-3}, batch size = 64) with a ReduceLROnPlateau scheduler. The loss function is the L1 loss. Training is performed for 100 epochs, and the checkpoint with the lowest validation error is selected. The final outputs are de-normalized back to ppm before computing the coefficient of determination R^2 and mean absolute error (MAE). Detailed model specifications and training hyperparameters are summarized in Supplementary Table 9, and ablation studies are provided in Supplementary Table 10.

Hydrogen monitoring system circuit design

We developed a sensor monitoring circuit that integrates wireless power transfer and data communication to enable efficient acquisition and wireless back-transmission of the hydrogen sensor signal; the detailed schematic is provided in Supplementary Fig. 41. The master-side loop employs a high-efficiency Class-E inverter together with an SS compensation network, so as to achieve near-maximal power-transfer efficiency even under weak magnetic coupling. The slave-side loop is based on load-modulation techniques, which modulate the sensor information onto the backscatter link and transmit it to the master side without additional power consumption. On this basis, we implemented a closed loop for signal acquisition and processing. After energy reception and rectification, the slave-side signal is digitized by a 10-bit analogue-to-digital converter (ADS7868) from the hydrogen sensor output. On the master side, a field-programmable gate array (FPGA, XC7Z020-2CLG400I) drives the inverter to generate an 830 kHz square-wave excitation, while acquiring and processing the recovered sensor-modulated data from the demodulation circuit. The FPGA then controls the Bluetooth module to transmit the data to the mobile application. During device fabrication, both the circuit and PCB were designed using JLCEDA software (Supplementary Fig. 42). In addition, we developed a dedicated mobile application using the App Inventor platform to enable real-time reception and storage of the sensor data via a Bluetooth module, and installed the application on an Android-based smartphone (Supplementary Fig. 43).

Biological hydrogen production

The bacterial strain used in this study was Clostridium butyricum (CGMCC 1.5205), obtained from the China General Microbiological Culture Collection Center (CGMCC, Beijing, China). The strain was cultured in a modified tryptic soy broth (TSB) medium (Guangzhou Huankai Biotechnology Co., Ltd.), with a TSB concentration of 30 mg mL^{-1}. The medium was autoclaved at 121 °C for 30 min, and sterile defibrinated sheep blood (0.05 mL mL^{-1}, Changde

Bikeman Biotechnology Co., Ltd.) was added as required. First, 4 mL of C. butyricum glycerol stock stored at −80 °C was thawed in a 37 °C water bath for 10 min, and then aseptically inoculated into a fermentation bottle containing 50 mL liquid TSB (with the chip integrated inside the bottle cap, inoculum dilutions of 1:100 or 1:500). Nitrogen was purged for 10 min to remove air from the bottle, after which the bottle was sealed and incubated in a temperature-controlled incubator at either 20 °C or 37 °C, detailed cultivation conditions are provided in Supplementary Table 11. During cultivation, hydrogen generation in the bottle was monitored every 2 h using the sensor for 11 h, and the data were recorded. After cultivation, the measurements were cross-validated using a portable hydrogen detector (Shenzhen Xinhairui Technology Development Co., Ltd., PGD3-C-H2).

References

1. Dincer, I. & Aydin, M. I. New paradigms in sustainable energy systems with hydrogen. *Energy Convers. Manage.* **283**, 116950 (2023).
2. Onwuemezie, L. Overview and prospects of low-emissions hydrogen (H_2) energy systems: Roadmap for a sustainable H_2 economy. *Energy 360* **1**, 100008 (2024).
3. Hübert, T. et al. Hydrogen sensors–a review. *Sens. Actuators B: Chem.* **157**, 329-352 (2011).
4. Koo, W.-T. et al. Chemiresistive hydrogen sensors: fundamentals, recent advances, and challenges. *ACS Nano* **14**, 14284-14322 (2020).
5. Satyapal, S. Hydrogen and Fuel Cell Technologies Office Multi-Year Program Plan. U.S. DOE. Report No.: DOE/GO-102024-6266 (2024).
6. Lee, J. S. et al. Wireless hydrogen smart sensor based on Pt/graphene-immobilized radio-frequency identification tag. *ACS Nano* **9**, 7783-7790 (2015).
7. Lu, H. et al. Lagging hydrogen detection standardization threatens energy transition. *Nat. Sens.*, 1-4 (2026).
8. Zhang, C. et al. Rational Design and Fabrication of MEMS Gas Sensors With Long-Term Stability: A Comprehensive Review. *Adv. Sci.* **12**, e11555 (2025).
9. Tang, Z. et al. Wafer-Scale Integration of Metal Oxide Nanocrystals on Gas Sensor Chips via Direct Lithographic Patterning. *ACS Sens.* **10**, 5520-5527 (2025).
10. Liu, L. et al. Heteronanostructural metal oxide-based gas microsensors. *Microsyst. Nanoeng.* **8**, 85 (2022).
11. Deng, Y. et al. Tailoring Chemiresistive Nanomaterials Toward Integrated Circuit Compatible Fabrication of Gas Sensors. *Adv. Mater.*, e08411 (2025).
12. Li, Z. et al. Advances in designs and mechanisms of semiconducting metal oxide nanostructures for high-precision gas sensors operated at room temperature. *Mater. Horiz.* **6**, 470-506 (2019).
13. Xie, W. et al. Synthesis of ordered mesoporous metal oxides by solvent evaporation-induced cooperative assembly. *Nat. Protoc.*, 1-34 (2025).
14. Bulemo, P. M. et al. Selectivity in Chemiresistive Gas Sensors: Strategies and Challenges. *Chem. Rev.* **125**, 4111-4183 (2025).

15. Ren, Y. et al. Synthesis of orthogonally assembled 3D cross-stacked metal oxide semiconducting nanowires. *Nat. Mater.* **19**, 203-211 (2020).
16. Guo, M. et al. Fast-response MEMS xylene gas sensor based on CuO/WO_3 hierarchical structure. *J. Hazard. Mater.* **429**, 127471 (2022).
17. Lee, K. et al. Effect of sintering temperature on the electrical and gas sensing properties of tin oxide powders. *Ceram. Int.* **47**, 22794-22800 (2021).
18. Zhang, X. et al. Ultralow detection limit and ultrafast response/recovery of the H_2 gas sensor based on Pd-doped rGO/ZnO-SnO_2 from hydrothermal synthesis. *Microsyst. Nanoeng.* **8**, 67 (2022).
19. Zhang, Z. et al. Chemiresistive H_2S gas sensors based on composites of ZnO nanocrystals and foam-like GaN fabricated by photoelectrochemical etching and a sol-gel method. *Sens. Actuators B: Chem.* **393**, 134148 (2023).
20. Wang, C. et al. Biomimetic olfactory chips based on large-scale monolithically integrated nanotube sensor arrays. *Nat. Electron.* **7**, 157-167 (2024).
21. Horprathum, M. et al. Ultrasensitive hydrogen sensor based on Pt-decorated WO_3 nanorods prepared by glancing-angle dc magnetron sputtering. *ACS Appl. Mater. Interfaces* **6**, 22051-22060 (2014).
22. Moon, H. G. et al. All villi-like metal oxide nanostructures-based chemiresistive electronic nose for an exhaled breath analyzer. *Sens. Actuators B: Chem.* **257**, 295-302 (2018).
23. Zong, B. et al. Smart gas sensors: recent developments and future prospective. *Nano-Micro Lett.* **17**, 54 (2025).
24. Lee, K. et al. Smarter Sensors Through Machine Learning: Historical Insights and Emerging Trends across Sensor Technologies. *Adv. Funct. Mater.*, e19859 (2025).
25. Yang, R. et al. Ultrafast Hydrogen Detection System Using Vertical Thermal Conduction Structure and Neural Network Prediction Algorithm Based on Sensor Response Process. *ACS Sens.* **10**, 2181-2190 (2025).
26. Li, X. et al. Optimization of the mixed gas detection method based on neural network algorithm. *ACS Sens.* **8**, 822-828 (2023).
27. Luo, W. et al. Pulse-driven MEMS gas sensor combined with machine learning for selective gas identification. *Microsyst. Nanoeng.* **11**, 72 (2025).
28. Yue, X. et al. A Drosophila-inspired intelligent olfactory biomimetic sensing system for gas recognition in complex environments. *Microsyst. Nanoeng.* **10**, 153 (2024).
29. Shulaker, M. M. et al. Three-dimensional integration of nanotechnologies for computing and data storage on a single chip. *Nature* **547**, 74-78 (2017).
30. Oulhakem, O. et al. Effect of water intercalation into tungsten trioxide structure ($WO_3 \cdot xH_2O$)(x= 0, 1, 2): correlation between structure and photocatalytic performances. *J. Catal.* **427**, 115109 (2023).
31. Lu, Y. et al. Fabrication of a monoclinic/hexagonal junction in WO_3 and its enhanced photocatalytic degradation of rhodamine B. *Chin. J. Catal.* **37**, 349-358 (2016).
32. Szymanski, J. T. & Roberts, A. C. The crystal structure of tungstite, $WO_3 \cdot H_2O$. *Can. Mineral.* **22**, 681-688 (1984).
33. Ahmadi, M. et al. WO_3 nano-ribbons: their phase transformation from tungstite ($WO_3 \cdot H_2O$) to tungsten oxide (WO_3). *J. Mater. Sci.* **49**, 5899-5909 (2014).
34. Ahmadi, M. & Guinel, M. J.-F. Synthesis and characterization of tungstite ($WO_3 \cdot H_2O$)

nanoleaves and nanoribbons. *Acta Mater.* **69**, 203-209 (2014).
35. Darmadi, I., Nugroho, F. A. A. & Langhammer, C. High-performance nanostructured palladium-based hydrogen sensors—current limitations and strategies for their mitigation. *ACS Sens.* **5**, 3306-3327 (2020).
36. Wang, X., Meng, X. & Gao, W. Ultrahigh-response sensor based on hierarchical Pd-WO_3 nanoflowers for rapid hydrogen detection. *Sens. Actuators B: Chem.* **387**, 133790 (2023).
37. Chen, H. et al. Co-infiltration and dynamic formation of Pd_3ZnC_x intermetallic carbide by syngas boosting selective hydrogenation of acetylene. *Nat. Commun.* **15**, 9850 (2024).
38. Garcia-Sanchez, R. F. et al. Thermal effects associated with the Raman spectroscopy of WO_3 gas-sensor materials. *J. Phys. Chem. A* **117**, 13825-13831 (2013).
39. Gu, F. et al. Atomically dispersed Pt (II) on WO_3 for highly selective sensing and catalytic oxidation of triethylamine. *Appl. Catal. B: Environ.* **256**, 117809 (2019).
40. Li, T. et al. PdO-resisted oxidation and enhanced hydration promotion of nitrogen electrooxidation to nitrate. *eScience*, 100473 (2025).
41. Ma, M. et al. Dual oxygen and tungsten vacancies on a WO_3 photoanode for enhanced water oxidation. *Angew. Chem.* **128**, 11998-12002 (2016).
42. Ismail, E. et al. Green palladium and palladium oxide nanoparticles synthesized via Aspalathus linearis natural extract. *J. Alloys Compd.* **695**, 3632-3638 (2017).
43. Do, V. H. et al. Pd–PdO nanodomains on amorphous Ru metallene oxide for high-performance multifunctional electrocatalysis. *Adv. Mater.* **35**, 2208860 (2023).
44. Yue, S. et al. Redox dynamics and surface structures of an active palladium catalyst during methane oxidation. *Nat. Commun.* **15**, 4678 (2024).
45. Li, J. et al. Essential role of lattice oxygen in hydrogen sensing reaction. *Nat. Commun.* **15**, 2998 (2024).
46. Ahmad, N. et al. Recent Advances on the Gas-Sensing Properties and Mechanism of Perovskite Oxide Materials-A Review. *ACS omega* **10**, 13780-13796 (2025).
47. Cho, S. H. et al. Substantially accelerated response and recovery in Pd-decorated WO_3 nanorods gasochromic hydrogen sensor. *Small* **20**, 2309744 (2024).
48. Qian, Y. et al. Hydrogen sensing with high-performance via O-ion spillover at Pd single atoms stabilized SnO_2 interface. *Commun. Mater.* **6**, 137 (2025).
49. Nie, Y. A Time Series is Worth 64Words: Long-term Forecasting with Transformers. *arXiv preprint arXiv:2211.14730*, (2022).
50. Li, M. et al. Research on prediction model of mixed gas concentration based on CNN-LSTM network. *Proceedings of the 3rd International Conference on Advanced Information Science and System* 1-5 (2021).
51. Vaswani, A. et al. Attention is all you need. *Adv. Neural Inf. Process. Syst.* **30**, (2017).
52. Yang, J. et al. AI-enabled portable e-nose regression predicting harmful molecules in a gas mixture. *ACS Sens.* **9**, 2925-2934 (2024).
53. Xiong, R. et al. On layer normalization in the transformer architecture. *PMLR* 10524-10533 (2020).
54. Chu, S. & Majumdar, A. Opportunities and challenges for a sustainable energy future. *Nature* **488**, 294-303 (2012).
55. Fu, Q. et al. Towards hydrogen production from waste activated sludge: Principles, challenges and perspectives. *Renew. Sustain. Energy Rev.* **135**, 110283 (2021).

56. Zhang, Q. et al. Biological fermentation pilot-scale systems and evaluation for commercial viability towards sustainable biohydrogen production. *Nat. Commun.* **15**, 4539 (2024).
57. Zhao, L. et al. Residue cornstalk derived biochar promotes direct bio-hydrogen production from anaerobic fermentation of cornstalk. *Bioresour. Technol.* **320**, 124338 (2021).
58. Jia, P. et al. Gas concentration prediction based on temporal attention mechanism in temporal convolutional networks. *Sens. Actuators B: Chem.* **433**, 137562 (2025).
59. Hendrycks, D. Gaussian Error Linear Units (Gelus). *arXiv preprint arXiv:1606.08415*, (2016).
60. Loshchilov, I. & Hutter, F. Decoupled weight decay regularization. *arXiv preprint arXiv:1711.05101*, (2017).

Acknowledgements

This work was supported by the National Key Research and Development Program of Ministry of Science and Technology (Grant No. 2023YFD2100305), National Natural Science Foundation of China (No. 62474059, 62474060), Fundamental Research Foundation of National Key laboratory of Automatic Target Recognition (No. WDZC20255290210), Huxiang Young Talents Program (No. 2023RC3105, 2024RC3075), Project of Yuelushan Center for Industrial Innovation (No. 2025YCII0109).

Author Contributions

S.X., J.Z., and L.S. conceived and designed the experiments. S.X., L.S., and Q.L. provided guidance and overall supervision of the project. J.Z., T.M., and X.T. were responsible for various nanometal-oxide fabrication processes. J.Z., Z.S., and Z.Z. fabricated the sensor devices. J.Z., J.D., Y.L., T.M., X.T., and M.Z. performed device characterization and collected/analyzed the sensing data. S.Z. and S.L. completed all deep-learning work. S.X., J.Z., H.L., W.D., R.L., S.D., and L.S. designed the biohydrogen demonstration experiment and the self-powered wireless transmission module. L. C. performed the related theoretical calculations. L.L., Y. W., C.W., R.L., S.D., and X.W. participated in discussions related to the manuscript. J.Z., S.X., Q.L., and L.S. wrote the manuscript. All authors discussed the results and reviewed the manuscript.

Competing Interests

The authors declare no competing interests.

Supplementary Files

This is a list of supplementary files associated with this preprint. Click to download.

- Supplementaryvideo.mp4
- SupplementaryinformationSubmitFinal202604071.pdf